On the elaboration of composite AlSi_7Mg_0.6/SiC powders and parts by laser powder bed fusion

Marie-Reine Manlay, Jean-Paul Garandet, Gatien Bacchetta, Mathieu Soulier, Camille Flament

On the elaboration of composite $AlSi_7Mg_{0.6}$/SiC powders and parts by Laser Powder Bed Fusion

Authors: MANLAY Marie-Reine[a,*], GARANDET Jean-Paul[a], BACCHETTA Gatien[a], SOULIER Mathieu[a], FLAMENT Camille[a]

[a]Univ Grenoble Alpes, CEA, LITEN, DTNM, F-38000 Grenoble, France
*Corresponding author

E-mail address: marie-reine.manmay@cea.fr (M-R. Manlay)

Journal of Materials Science
DOI: 10.1007/s10853-023-08249-1

Abstract

The present work focuses on the development of Al/SiC materials manufactured by Laser Powder Bed Fusion (L-PBF). More specifically, our goal is to address the issue of the SiC dissolution kinetics, with the objective of preventing or at least limiting SiC decomposition into Al_4C_3 in melted aluminum. To do so, Al/SiC powder composites with SiC particles of various sizes, namely from circa 35 nm to 4.5 µm, using a standard $AlSi_7Mg_{0.6}$ alloy as host material are first successfully prepared, and these composite powders are printed in a standard L-PBF equipment. The resulting parts are then thoroughly characterized. An important result is that only the largest 4.5 µm particles can be partially preserved. These findings are consistent with the results of a diffusion based numerical model, which allows in addition to study the kinetics of powder dissolution as a function of thermophysical and process parameters. A general finding of the present work is that a thermodynamically unstable nanoparticle cannot survive the L-PBF process.

Keywords: Laser Powder Bed Fusion, $AlSi_7Mg_{0.6}$/SiC composite, SiC decomposition, Al_4C_3, Diffusion

1. Introduction

Additive manufacturing (AM) refers to a number of materials fabrication technologies allowing to build parts layer by layer to Net Shape (or at least Near Net Shape) according to a prescribed computer file. AM allows faster prototyping, weight reduction thanks to topological optimization, component customization, the production of complex shapes or the reduction of the number of assembly steps compared to conventional manufacturing processes. AM is in continuous industrial expansion, and it addresses virtually all types of markets, e.g. energy, aeronautics, oil and gas, medical and health care, luxury. Among AM methods, Laser Powder Bed Fusion (L-PBF) offers a strong potential to manufacture three-dimensional dense parts with complex geometries, which could not be obtained in one-step by conventional processing routes. The L-PBF technique is based on the deposition of successive powder layers, which are selectively melted by a laser according to a previously established computer-aided design (CAD) file. L-PBF is used for the elaboration of several metallic materials, in particular aluminum alloys, see e.g. [1] for the potential of the technique.

Aluminum is a widely used metal in many industrial fields due to its very interesting properties, especially in terms of weight reduction and corrosion resistance. In order to improve its mechanical properties, a common strategy is to add alloying elements to the base metal. According to the material application, and thus the target performance, aluminum alloys can be reinforced in several ways: either post-production, by applying an age hardening, leading to the formation of needle-shape β" nano-precipitates in Al-Mg-Si alloys of the 6xxx series [2] or during elaboration, by adding reinforcements to form aluminum-based metal matrix composites, which make it possible to combine the properties of several materials [3]. SiC particles are an adapted candidate to reinforce aluminum alloys thanks to their low density, high hardness and high elastic modulus. Many studies focus on the development of Al/SiC composites by stir casting [4], e.g. Duralcan composite [5], or Spark Plasma Sintering (SPS) [6]. Spectacular results were notably obtained by X. Li et al., who greatly improved the yield strength of an A356 alloy by adding only 1 wt% of SiC nanoparticules [4]. These composites are used in the automotive, aerospace and defense industries, in particular for the production of brake discs, drive shafts and helicopter blade rotors.

Literature reports a well known technical issue in the manufacturing process of such composites: the instability of SiC in molten aluminum occurring above 660°C according to the following reaction: $4Al(l) + 3SiC(s) \rightarrow Al_4C_3(s) + 3Si(s)$ [7]. Gröbner et al. [8] described the thermodynamic calculations in the Al-Si-C ternary system, showing the instability of SiC in liquid aluminum leading to the formation of Al_4C_3. In addition to the degradation of the mechanical properties, the presence of the aluminum carbide Al_4C_3 is expected to reduce the aluminum composite parts lifetime, as this carbide phase is soluble in water or in humid atmosphere [9]. From a material standpoint, a potential solution to address this issue is to enrich the matrix with silicon, in order to delay or block the reaction, taking into account the fact that the amount of Si required to saturate the melt increases with temperature. For instance, L. Salvo et al. [10] grouped the results of different authors in order to display the limit Si concentration required to SiC stability from 900 to 1400 K. This shows that the critical Si content to inhibit the decomposition reaction is around 16 wt% at 1400K. Due to the high temperatures reached by the material during L-PBF process, it can thus be expected that the necessary amount of silicon would be very high, which is not desirable since it would completely modify the composition of the aluminum alloy.

From a process standpoint, this issue of silicon carbide dissolution can be managed in the conventional manufacturing techniques of these composites as the maximum temperatures reached can be at least to some extent controlled, but the much higher process temperatures reached in L-PBF will enhance the reactivity between the aluminum matrix and the silicon carbide reinforcements. It thus appears that some SiC dissolution will be unavoidable in the L-PBF process. However, the extent of the dissolution process needs to be clarified, since the literature reports a number of a priori conflicting findings [11–18].

In this context, the purpose of the present work is to address the issue of the SiC dissolution kinetics, with the objective of preventing or at least limiting SiC decomposition into Al_4C_3. To do so, our methodology is as follows: we first prepare Al/SiC composites with SiC particles of various sizes, namely from circa 35 nm to 4.5 µm, using a standard $AlSi_7Mg_{0.6}$ alloy as host material. As opposed to structural Al alloys (e.g. Al 6061 or Al 7075), which are known to be prone to hot cracking, this widely used $AlSi_7Mg_{0.6}$ grade can be readily printed to yield fully dense parts on standard equipment. After SiC grafting on the $AlSi_7Mg_{0.6}$ host particles, the composite powders is thoroughly characterized before fabrication. Regarding the printing step, various process parameters, covering a large range of energy densities, are investigated. The

samples (cubes of 1 cm² cross section) are then thoroughly characterized using a variety of techniques.

Regarding the organization of the manuscript, the materials and methods used to perform this research work are detailed in section 2. The results obtained are then presented and analyzed in section 3, and a relatively simple diffusion controlled kinetic dissolution model allowing to account for the experimental results is proposed in section 4. Finally, section 5 is dedicated to a discussion of the findings, providing general clues regarding the elaboration of Al/SiC composites by L-PBF.

2. Experimental procedure

2.1. Raw materials

The host material used in this study is gas atomized spherical $AlSi_7Mg_{0.6}$ powder acquired from TLS Technik GmbH & Co. The particles have a range size of 15-53 µm and a median diameter of 29 µm. Their chemical composition is reported in Table 1. The material density, as measured by Helium pycnometry, is 2.66 $g.cm^{-3}$.

Composition	Al	Si	Mg	Fe	Cu	Zn	Ti	Mn
Specification	Bal.	6.50-7.50	0.45-0.70	≤0.19	≤0.05	≤0.07	0.08-0.25	≤0.10
Powder	Bal.	7.23	0.62	0.18	0.005	<0.001	0.18	0.003

Table 1: Chemical composition of the $AlSi_7Mg_{0.6}$ alloy powder (wt%)

As mentioned in the introduction, the objective of the present work is to study to which extent SiC can survive the L-PBF process by using different sized SiC particles, respectively with a mean size of 35 nm, 750 nm, 2 µm, and 4.5 µm. Nanoparticles of 35 nm were produced by laser pyrolysis and provided by Nanomakers. Larger particles were produced by the Acheson method and provided by Washington Mills.

2.2. Composite powder elaboration

As mentioned in introduction section, 1 wt% of SiC is enough to greatly improve the parts mechanical properties [4]. For this study, the amount of reinforcement particles was fixed at 3 wt%, mostly with the objective to facilitate XRD analysis without imposing a too significant modification of the starting $AlSi_7Mg_{0.6}$ composition. Composite powders mixtures with 3 wt% of reinforcement are elaborated using two different mixing procedures. The first relies on the use of a tridimensional mixer (Turbula) coupled with zirconia milling balls, in order to perform dry coating of reinforcements on matrix particles. Dry coating is based on an electrostatic assembly of nanoparticles at the surface of micrometric powders [19]. The potential of this approach to develop composite powders for the LPBF process has already been demonstrated, for different mixers [20]. The mixture is performed in a 2.25 L borosilicate vial, with two sizes of zirconia balls (10 mm and 2 mm) and a ball to powder ratio of 4. The amount of Al alloy powder introduced in the vial is 937.5 g with 29 g of SiC. The duration of the mixing is set to 15 hours. For reasons that will become apparent in section 3, a more energetic mixing was found to be necessary for the highest 4.5 µm reinforcement size. Therefore, a 5 L capacity Cyclomix high-shear impact mixer has been used in that case. As the container volume is larger, the Al alloy amount is set to 2.5 kg, for 77 g of SiC to respect the 3 wt% target. Rotation speed was 15 $m.s^{-1}$, and mixing duration 30 minutes.

Composite powders properties are investigated through several characterization techniques. Powders granulometry is measured using static image analysis (Malvern Morpho G3), allowing to give information on the electrostatic mixture stability. The analysis is performed on 150000 particles at a x20 magnification with a detection limit for particles smaller than 1 µm. The quality of electrostatic assembly of powders is also evaluated by Scanning Electron Microscopy (SEM) using a Field Emission Gun (FEG) SEM Zeiss Merlin. For the determination of mass balances, Instrumental Gas Analysis (IGA) analysis, performed by Elektrowerk Weisweiler GmbH, was also used through 0.3-0.4 g specimens for analysis of carbon content.

2.3. Laser Powder Bed Fusion process

Bulk composites are produced by Laser Powder Bed Fusion with a SLM Solutions machine (SLM 125 HL), equipped with a 400 W laser and a spot diameter of 70 µm, under Argon

atmosphere. For each composite powder, 1 cm^3 cubes were printed. For all cubes, several parameters are kept constant: hatch distance (h) of 0.17 mm, layer thickness (t) of 50 µm, substrate temperature at 160°C. Lasing strategy is implemented in stripes, with a rotation of the scan direction by 33° from layer to layer. A parametric study on scan speed (v) and laser power (P) is carried out, respectively varying from 800 $mm.s^{-1}$ to 1600 $mm.s^{-1}$ and from 275 W to 375 W, as presented in Table 2. From these parameters, a volumic lasing energy is determined using Eq.1.

$$E = P/(v.h.t) \quad (1)$$

From a physical standpoint, it would make sense to include an absorptivity coefficient in eq. (1), but the latter is not easy to estimate. It should also be noted that other definitions for the energy density, featuring the laser spot size can be found in the literature, see [21] for a detailed discussion of this important issue. Even though the formulation of eq. (1) cannot be expected to capture the local physics of the heat transfer phenomena, it is used here for purposes of comparison with literature data. Process parameters are set according to manufacturer indications and the volumic lasing energy conforms with literature practices on the same aluminum alloy [14, 22–24].

Power Speed	275 W	300 W	325 W	350 W	375 W
800 $mm.s^{-1}$	40.4	44.1	47.8	51.5	55.1
1000 $mm.s^{-1}$	32.4	35.3	38.2	41.2	44.1
1200 $mm.s^{-1}$	27.0	29.4	31.9	34.3	36.8
1400 $mm.s^{-1}$	23.1	25.2	27.3	29.4	31.5
1600 $mm.s^{-1}$	20.2	22.1	25.7	25.7	27.6

Table 2: Lasing energies ($J.mm^{-3}$) for the parameters applied at each cube according to the variation of scan speed and laser power

Density of bulk composites is measured by Archimedes' principle in ethanol. For details on this well known technique, the interested reader is referred to A. B. Spierings et al. [25] and T. de Terris et al. [26]. The fabricated samples are then characterized by means of X-Ray Diffraction (XRD) (Brüker D8 Advance) with a variation of 2θ angle from 28° to 42° in order to identify the different phases constituted the composite. Fine microstructure such as submicron precipitation was observed thanks to Transmission Electron Microscopy. TEM analysis are

performed using a FEG Tecnai Osiris from Thermofisher operating at 200 kV. The images are recorded by conventional TEM, or by S-TEM with High Angle Annular Dark Field (HAADF) and Bright Field (BF) detectors. Energy Dispersive X-rays spectroscopy (EDX) data are acquired in STEM mode with the super-X detector from Brüker equipped with four Silicon Drift Detectors. Samples for TEM analyses are prepared using a cross-beam Focused Ion Beam 550 from Zeiss (FIB). TEM lamella is lifted out according to the perpendicular plane to building direction.

3. Results

3.1. Composite powders characterization

A first criterion to assess the homogeneity of the mixture is to use the carbon IGA measurements in composite powder samples and to compare the obtained results with the theoretical quantity of carbon introduced into the mixture, namely 0.9 wt%. Indeed, considering the amount of C in the starting $AlSi_7Mg_{0.6}$ powder to be negligible, a measurement of the carbon content in composite powder samples allows to determine the mass fraction of SiC in composite powder. Table 3 displays the IGA results for Carbon content in the different composite powders.

	Al/SiC 35 nm	Al/SiC 750 nm	Al/SiC 2 µm	Al/SiC 4.5 µm
Powder (wt%)	0.83	0.51	0.27	0.81
Mixing method	Turbula	Turbula	Turbula	Cyclomix

Table 3: Analysis of carbon content in the composites powders

The first conclusion that can be drawn is that the amount of C measured, and thus the amount of SiC on the starting $AlSi_7Mg_{0.6}$ powder strongly decreases with particle size for the mixtures at 35 nm, 750 nm and 2 µm that were performed in the Turbula mixer. This was expected, since it is known from the literature [27], [28] that the size of the reinforcements has an impact on their ability to be electrostatically assembled, and to this end nanosized guest particles are commonly used. This composite powder segregation was partially overcome using the high energy Cyclomix mixer for the largest reinforcement size of 4.5 µm, allowing a better mixing homogeneity compared to Turbula.

In any case, the amount of SiC incorporated on the surface of the host $AlSi_7Mg_{0.6}$ powder is thus quite different between the various reinforcements sizes. This mixing efficiency issue would require a mixing process optimization for industrial applications, but not for a study aiming at checking whether SiC particles can survive the L-PBF process. Indeed, what matters for the purposes of the present work is the fact that whatever the mixing device a sufficient amount of SiC is incorporated, so that its becoming during the printing process can be studied.

To go deeper into characterization of the composite powder, let us recall that our objective is to achieve a homogeneous electrostatic assembly of the reinforcement particles on the surface of the aluminum particles. A first possible way to qualitatively characterize the electrostatic assembly is to observe composite powders by SEM. According to SEM images presented in Figure 1, the nano-SiC of 35 nm seems to completely cover the aluminum particles surface by a cottony appearance. The 750 nm SiC particles were partially assembled, but uncovered parts are still visible. In the case of 2 µm and 4.5 µm SiC, only a few reinforcements are detected.

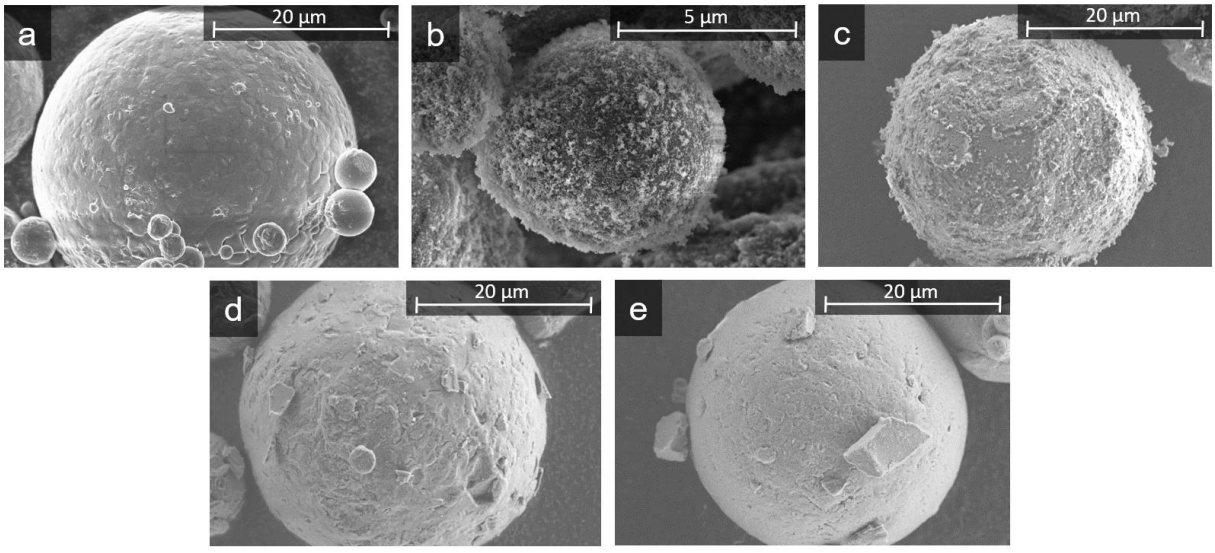

Fig. 1 SEM images of the powders: $AlSi_7Mg_{0,6}$ matrix raw powder (a), Composite Al/SiC 35 nm (b), Composite Al/SiC 750 nm (c), Composite Al/SiC 2 µm (d), Composite Al/SiC 4.5 µm (e)

Another possible way to qualify this assembly is based on granulometry measurements. For such measurements, a monomodal distribution corresponding to the granulometry of aluminum alloy powder would testify of a complete electrostatic coating, while a bimodal dispersion would indicate an incomplete assembly with a second peak corresponding to the signature of remaining unbound reinforcements. However, it should be kept in mind that due to possible

particle agglomeration, a peak associated to unbound particles may be shifted towards higher size ranges as compared to the individual reinforcement particles.

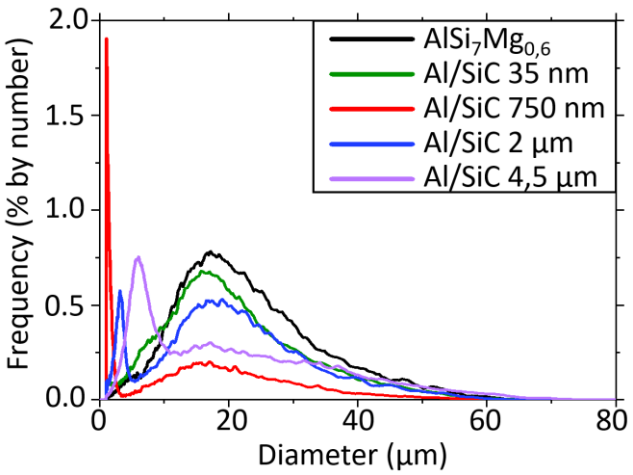

Fig. 2 Composite powders size distribution: SiC particle size influence on electrostatic assembly

Figure 2 presents the results of granulometry measurements for the different composite mixtures elaborated. No additional peak is detected for the nanocomposite with 35 nm SiC reinforcements that presents a monomodal dispersion. Keeping in mind the filtering used in the morpho-granulometry analysis (see section 2.2), the absence of such a peak does not by itself guarantee that all reinforcement particles were indeed grafted on the host particles. Nevertheless, in connection with the results of the IGA and SEM characterizations, our claim is that the 35 nm reinforcement particles have been properly coated.

Regarding the larger reinforcement sizes, Figure 2 brings evidence of an incomplete coating with a bimodal distribution in the case of the 750 nm, 2 µm and 4.5 µm SiC particles, with the peaks in the 1-5 µm range corresponding to SiC, and the main peak to the Al-based alloy. At a given wt% reinforcement addition as used in the present work, the number of added SiC particles decreases with size, therefore the relative intensities between the reinforcement peaks are not comparable.

Thus an overall consistency can be found in all the obtained results. The Al/SiC 35 nm composite powder is homogeneous, while the mixtures with the 750 nm and 2 µm reinforcements show a silicon carbide content lower than expected, due to an incomplete assembly, especially in the case of 2 µm reinforcement. This is in line with the SEM images of the composite powders, on which it can be noted that very few 2 µm reinforcements have been assembled on the surface of the aluminum powders. The Al/SiC 4.5 µm mixture has been

elaborated with the Cyclomix mixer, a better carbon content is obtained, which confirms that a more energetic mixer is more effective for large reinforcements.

3.2. Process characterization

The composite powders are then printed by L-PBF according to a parametric study by varying the laser power or the scan speed for each cube. Twenty-five bulk composites are thus obtained for each powder, each with a different lasing energy density. IGA measurements are performed on the bulk composites in order to control the effective amount of SiC present in the final composite. Table 4 presents the IGA results for the carbon content analysis measured on the denser cubes of the fabrication plate, and the expected amount of SiC measured in the powder mixture. Regarding the 35 nm, 750 nm and 4.5 µm reinforcements, the slight discrepancies between bulk and powder compositions can be considered to remain within the measurement uncertainties (0.05-0.1 wt%), that is associated to both the IGA technique error bars and the limited number of samples tested. On the other hand, the discrepancy is significant for the 2 µm reinforcement case, testifying again of a rather poor grip of the SiC on the host particles and of a heterogeneous mixture.

	Al/SiC 35 nm	Al/SiC 750 nm	Al/SiC 2 µm	Al/SiC 4.5 µm
Bulk (wt%)	0.89	0.57	0.14	0.89
Powder (wt%)	0.83	0.51	0.27	0.81

Table 4: Analysis of carbon content in the composites parts

Figure 3 displays the relative density of the cubes printed with different lasing energies for each composite with different reinforcement sizes, i.e. 35 nm, 750 nm, 2 µm and 4.5 µm, obtained by Archimedes' principle in ethanol. Solid lines are only guide to the eyes, obtained from the fitting of the data with a third order polynomial. Also shown in Figure 3 is the reference $AlSi_7Mg_{0.6}$ alloy printed with the same parameters. An important issue to mention is that the theoretical density of our Al/SiC composites is unknown due to the various reactions occurring during the process. For want of a better method, it has been estimated here using a volume additivity hypothesis. Anticipating on the results shown later on, the density of the 35 nm, 750 nm, 2 µm composite samples was calculated assuming that all the SiC content in the powder

has been transformed into Al_4C_3. For the 4.5 µm sample it was assumed quite arbitrarily that half the amount of SiC had been transformed into Al_4C_3.

Too much emphasis should therefore not be laid on the quantitative values reported, our purpose with the presentation of the results in Figure 3 is to show that our process is reasonably well controlled, with the possibility of reaching low porosity levels, and density curves following a well-known trend from lack of fusion to keyhole porosities [29]. Indeed, all curves have the classic bell shape obtained in L-PBF parametric studies, in our case with a maximum in the energy density range between 25 and 35 J.mm^{-3}.

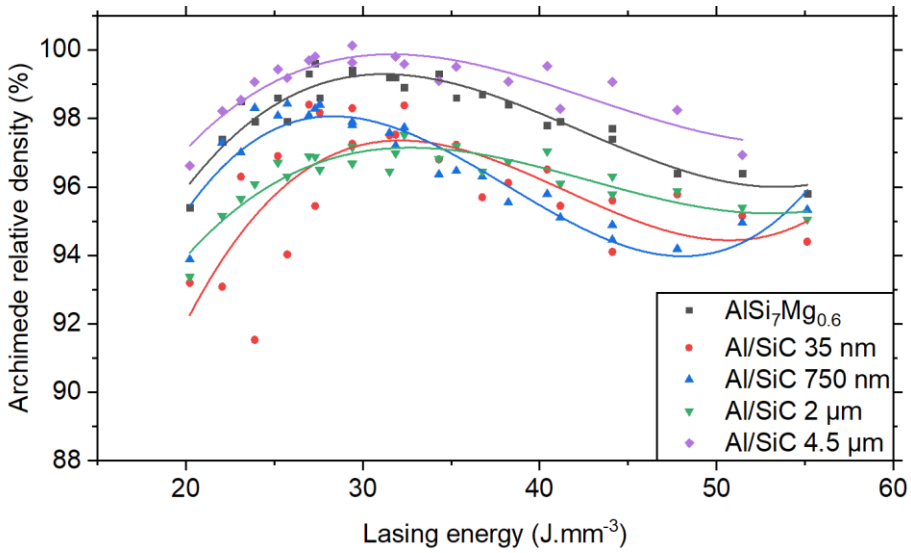

Fig. 3 Archimedes' density of composites

Reference material can reach a near full density between 25 and 35 J.mm^{-3}, which conforms with literature, while the maximum density for the four other materials is between 97% and 100%. The results underline that the addition of reinforcements raises a number of issues. Apart from the uncertainty on the reference mass densities to be used mentioned above, this loss of density could be explained by different contributions: first, many more ejecta are experimentally observed when printing composites compared to the reference material, showing that the process is less stable than without reinforcements. This is especially true at high lasing energies where the melt pool turbulence could be strong. Another explanation is that the addition of SiC decreases wettability and can lead to a balling effect, thus reducing densification [15].

The results from the Archimedes measurement correlate well with the SEM observations presented in Figure 4. At low lasing energies, characteristic large, irregular lack of fusion porosities, featuring trapped unmelted powder can be evidenced. On the other hand, at high lasing energies, large inert spherical gas pores, likely due to the keyhole effect, contribute to the loss of density [30, 31].

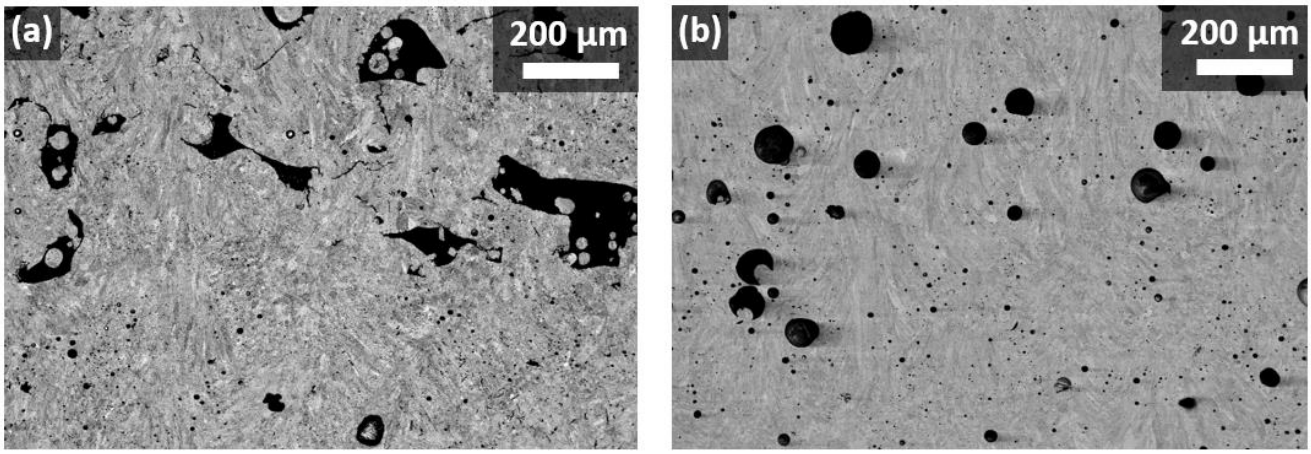

Fig. 4 SEM images of the porosities in the composite $AlSi_7Mg_{0.6}$/SiC 750 nm: lack of fusion at 20.2 J.mm^{-3} (a), keyhole at 55.1 J.mm^{-3} (b)

It should be stated that porosities remain present even in samples with the highest mass densities pointing to potential issues in material and/or process control. However, these issues can be considered as relatively minor in view of the attained densities. Even more important, in a study focused on the becoming of SiC particles, a full mastery of the composite powder printing process is not of primary importance, what matters most is the ability to detect remaining SiC particles.

3.3. Parts microstructure characterization

The obtained materials can be further characterized by XRD and TEM analysis, in order to identify the existing phases and to help understanding the involved reaction mechanisms. The results presented in Figure 5 were obtained on materials printed at 32.4 J.mm^{-3}, i.e. in the range yielding the maximum density of the matrix sample.

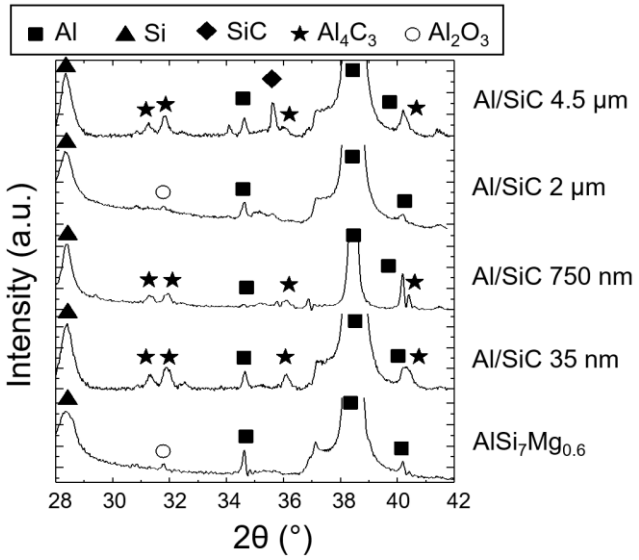

Fig. 5 Composite diffractograms for the each reinforcement size at 32.4 J.mm^{-3} lasing energy

The diffractograms show peaks characteristic of the Al_4C_3 phase, supporting the decomposition of SiC into Al_4C_3 for most of composites. A total decomposition occurs for composites with 35 nm and 750 nm reinforcements, as indicated by the signature of Al_4C_3 peak and the absence of SiC signature. The composite Al/SiC 2 µm presents a particular diffractogram since no carbide is detected. The absence of Al_4C_3 can not be associated to the preservation of the initial SiC, since SiC peaks are not observed. On the other hand, the relatively low amount of carbon incorporated see Tables 3 and 4, can be held responsible for such a finding, as the carbide amount is too low to be detected by XRD. Al/SiC 4.5 µm diffractogram shows simultaneously peaks corresponding to Al_4C_3 and SiC phases. That means that the reinforcement is large enough to allow some SiC to survive the L-PBF process, even if it has been partially decomposed. SEM observations support this statement. SiC particles are indeed observable and surrounded by rod-shaped Al_4C_3, as indicated on Figure 6.

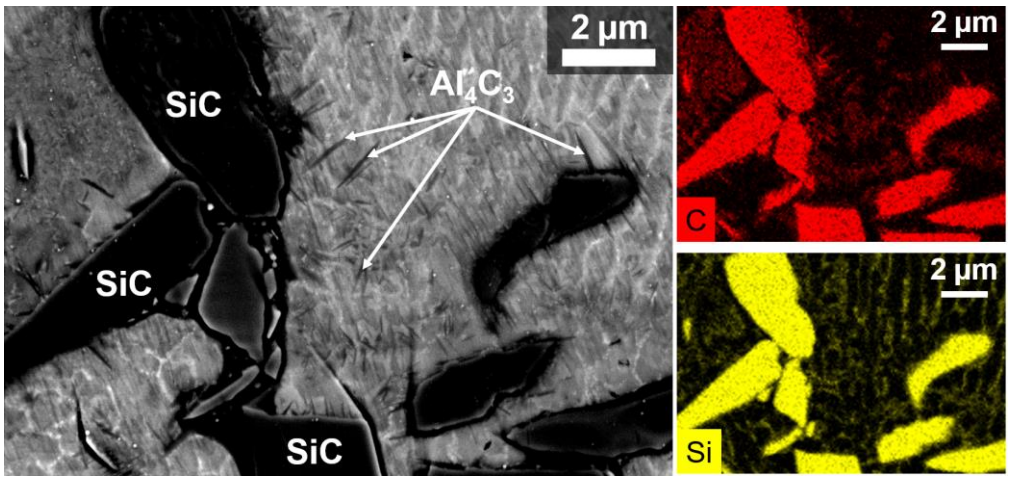

Fig. 6 SEM-EDX analysis of residual SiC particles after L-PBF process in the Al/SiC 4.5 µm composite printed at 32.4 J.mm^{-3}

Some analysis were also performed at a low lasing energy, i.e. 20.2 J.mm^{-3}, presented in Figure 7. Peaks associated with SiC can be identified with those pertaining to Al_4C_3 in the diffractograms. However, it is likely that the observed SiC peaks come from unmelted particles in lack of fusion porosities, and therefore cannot be associated to a true survival of SiC in the liquid phase. Thus, even if SiC can be preserved at low energy density levels, the situation is not interesting for an application point of view because these materials are far away from being dense.

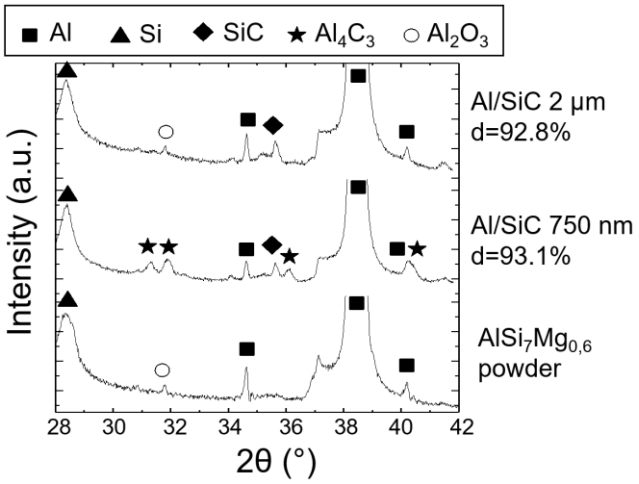

Fig. 7 Composite diffractograms for the 750 nm and 2 µm reinforcements at 20.2 J.mm^{-3} lasing energy

TEM analysis were performed in order to observe the precipitation in the composite Al/SiC 35 nm. EDX maps do not reveal the presence of silicon carbide for the nanocomposite materials. On the other hand, the presence of rod shaped aluminum carbide Al_4C_3 randomly located at grain boundaries is detected by EDX, as shown in Figure 8, and by measuring the lattice parameter using High Resolution TEM (HRTEM) (Figure 9). These inclusions are surrounded by pure silicon precipitates, which are the other reaction product of the silicon carbide decomposition.

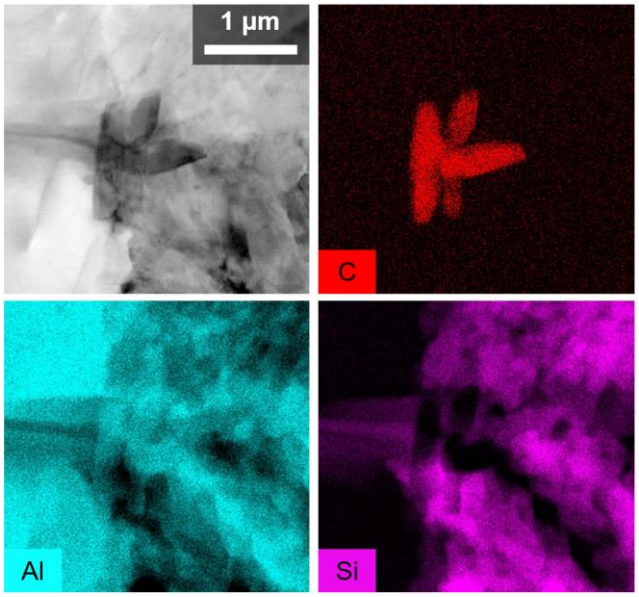

Fig. 8 TEM-EDX analysis of rod shaped Al_4C_3 inclusions surrounded by Si precipitates in the composite Al/SiC 35 nm

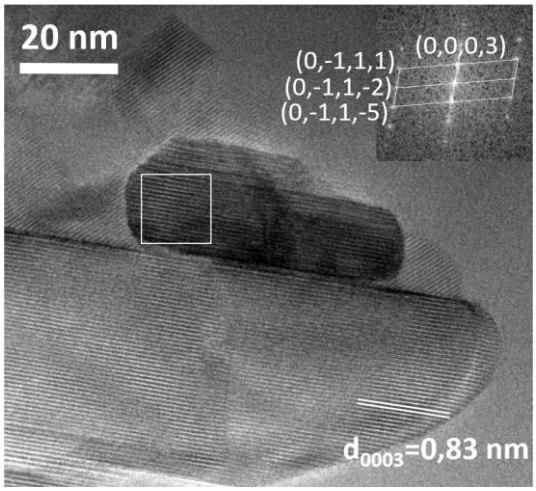

Fig. 9 HR-TEM observation of Al_4C_3 in Al/SiC 35 nm composite with its indexed Fourier transformation

Thus, submicronic SiC is not preserved, excepted at low lasing energies by the presence of unmelted particles due to lack of fusion, leading to poor densification of the parts. Regarding well consolidated samples, only the largest 4.5 µm SiC particles have partially survived the L-PBF process.

4. Diffusion based dissolution model

4.1. Methodology

Our objective in this section is to propose a relatively simple dissolution model to account for the fact that large SiC particles are able to survive the L-PBF process, whereas smaller ones fail to make it. We will only focus on diffusion related kinetics though fragmentation phenomena can also be active in the case of composite SiC particles [32]. If only diffusion is involved, the mass flux J in $kg.s^{-1}$ between a dissolving particle and its surrounding fluid medium is given by the following equation:

$$J = \rho.D.A.G_c \tag{2}$$

Where ρ is the mass density of the dissolving species ($kg.m^{-3}$), D the liquid phase diffusion coefficient ($m^2.s^{-1}$), A the area of the particle (m^2) and G_C the norm of the composition gradient (expressed in units of mass fraction per meter) within the fluid. From now on, we will focus on the behavior of the carbon species, since it can be considered that its concentration away from the dissolving particle is zero. In other words, the assumption is that the melt pool enrichment in carbon can be neglected. Another simplifying hypothesis is that the particles will be considered spherical.

Provided the diffusion coefficient of carbon in the liquid alloy could be estimated, it would seem to be a relatively simple task to estimate the mass flux, and thus the mass loss by time integration to assess whether a particle of given size is expected to survive the process. However, apart from the mass density ρ, all other partakers in equation (2) depend on time. This is quite obvious for the particle area, since the dissolution process itself implies its decrease. But since a spherical shape is assumed, a mass loss can be easily traduced in a reduction of the particle radius.

As for the concentration gradient, even if the composition scale can be considered as fixed from the fact that both the carbon fraction in the dissolving SiC shell and the far field composition do not vary, the diffusion length scale is expected to increase along the dissolution process. Fortunately, an analytical solution for the composition field in spherical coordinates can be

found in text book literature [33]. For fixed interface C_I and far field C_∞ compositions, the time dependent solution can be expressed for a particle of radius R as:

$$G_C = (C_I - C_\infty)\,[R^{-1} + (\pi D t)^{-1/2}] \quad (3)$$

The value of the diffusion coefficient is an issue by itself since reliable literature data in liquid metals is scarce. This is due to a number of difficulties in realizing well controlled measurements in high temperature and chemically aggressive environments, but especially to the effect of mass transport associated to natural convection, hardly avoidable in practice, that is seen to often hide as accelerated diffusion [34, 35]. A number of interesting results have been obtained taking advantage of the good electrical conductivity of liquid metals and using magnetic fields to control convection [36–38], but unfortunately the number of investigated systems remains limited.

The issue of data reliability is especially acute in problems such as the one considered here where the temperature dependence of the coefficient needs to be taken into account, since large temperature variations are expected from the L-PBF process. Regarding the functional form D = f(T), results are often presented conventionally assuming an Arrhenius form, with a constant activation energy, see for instance the review for aluminum [39]. But a power law model with a T^2 dependence can also successfully fit the data [36].

Assuming the temperature dependence of the diffusion accounted for, the choice for the value to be used at a given time t_0 in eq. (2) is relatively straightforward, namely the instantaneous value of D at the actual temperature $T(t_0)$. But the situation is not so easy for eq. (3), as the length scale $(\pi D t)^{1/2}$ classically met in diffusive problems is a result of the thermal history of the process since D has varied between t = 0 and $t = t_0$. Fortunately, from a mathematical standpoint, the solution comes again from text book literature [33] that allows to derive temperature averages $D_{eq}(t_0)$ and $T_{eq}(t_0)$ defined as :

$$D_{eq}(t_0) = D(T_{eq}(t_0)) = (1/t_0) \int_0^{t0} D(t)dt, \quad (4)$$

which can be used to derive the length scale $(\pi D t)^{1/2}$ featured in eq.(3). However, we still have to come back on the issue of input data regarding our present problem of carbon diffusion in aluminum based liquid alloys. Unfortunately, we were not able to identify relevant data from

the literature. So the discussion will be mostly based on the review by Du et al. [39], that considered a large number of solutes both in face centered cubic structure and liquid Al. Regarding liquid phase behavior, it should be noted that the effect of the alloying elements in our $AlSi_7Mg_{0.6}$ on the transport properties (viscosity and diffusivity) can be significant. But back to Du et al. [39], the good news are that for most solutes, at a temperature T = 1000 K, values of D in the 3.10^{-9} $m^2.s^{-1}$ – 7.10^{-9} $m^2.s^{-1}$ appear rather reasonable to be used as starting guesses for a parametric study.

Regarding the temperature dependence, for most solutes, the Arrhenius law activation energies in Du et al. [39] range between 20 and 30 $kJ.mol^{-1}$. For a temperature of 2000 K, this amounts respectively to a 3.3 and 6.1 fold increase with respect to the 1000 K reference. Incidentally, for a T^2 power law dependence, the increase between 1000 K and 2000 K is of a factor 4. These are obviously significant differences, but for a semi quantitative approach, they are small enough for a parametric study to make sense.

Besides, since the days of Du et al. review [39], a number of papers presenting reliable data in Al based systems were published, see for instance [40–42]. At 1000 K, values close to D = 7.10^{-9} $m^2.s^{-1}$ for the self-diffusion of Al [40], and to D = 3.10^{-9} $m^2.s^{-1}$ and D = 5.10^{-9} $m^2.s^{-1}$ respectively for the interdiffusion coefficients in Ni [41] and Cu [42] doped Al based alloys were reported. As for activation energies, the reported values of 280 meV (amounting to 27 $kJ.mol^{-1}$) for Al self-diffusion [40] and 247 meV (amounting to 24 $kJ.mol^{-1}$) for the interdiffusion coefficient in Al rich Al-Ni alloys [41] fit well within the previously mentioned 20 to 30 $kJ.mol^{-1}$ range.

Even in the absence of dedicated experiments for the measurement of carbon diffusivity in $AlSi_7Mg_{0.6}$, the relative coherence of the literature data supports the possibility of carrying out a parametric study for our present semi-quantitative purposes. As for reference diffusion coefficient at 1000 K, values between D = 3.10^{-9} $m^2.s^{-1}$ and D = 7.10^{-9} $m^2.s^{-1}$ will be tested. As for temperature dependence, most of the simulations were carried out with the T^2 power law, but a number of cases were also run using the Arrhenius law.

Last but not least, we still have to specify the time-temperature profiles experienced by a SiC particle in a L-PBF melt pool. Very interesting in this respect is the numerical modelling work of Li and Gu [43] who focused on a related $AlSi_{10}Mg$ alloy. Depending on the process

parameters, maximum temperatures and melt pool durations up to almost 2000 K and 1 ms were attained. However, it should be recalled that the thermal history at a given spatial location is expected to vary significantly, as demonstrated by Loh et al. on a related Al 6061 alloy [44]. Therefore we will in the following parametric study consider model time temperature profiles starting at T_{Ref} = 940 K (i.e. the thermodynamic dissolution temperature of SiC) at t = 0, increasing linearly to a temperature T_{Max} at t = t_{Max} and from there decreasing linearly back to T_{Ref} at t = t_{End}. There is obviously no physical reason for the profiles to be linear, but in view of the numerous assumptions of the model this should not matter. Besides, it should be noted that in generally $t_{End} > 2\ t_{Max}$ since cooling is expected to be slower than heating.

With all the model ingredients at hand, we can now turn to a presentation of the results. For the interested reader, more details on the numerical implementation of the model can be found in Appendix 1. Let us recall once more that in view of the numerous assumptions, the model cannot be expected to be quantitatively predictive, but our claim is that it will nevertheless allow for a number of general conclusions to be drawn.

4.2. Simulation results

The first parameter to test is the SiC particle size, as it has been experimentally studied in this work, with particles size of 35 nm, 750 nm, 2 µm, 4.5 µm, i.e. the mean size of SiC powders used in experimental study. In this first set of simulations, the diffusion coefficient at 1000 K is voluntarily chosen in the lower value range, namely 3.10^{-9} $m^2.s^{-1}$, to set a higher bound on SiC preservation. As for the other parameters, their values (T_{max} = 1500 K, t_{End} = 500 µs and t_{max} = 200 µs) are taken as representative of average process conditions. The results are summarized in Figure 10, which shows the diameter evolution of particles during the temperature cycle.

It is clear from Figure 10 that only the 4.5 µm sized particle can be partially preserved in a typical temperature cycle. A 2 µm SiC particle is totally consumed after about 200 µs, and a 750 nm SiC particle after about 50 µs. For a truly nanometric 35 nm SiC particle, it is consumed in a few µs, this is why the curve corresponding to its size evolution is not visible on the graph. This last result shows that a SiC nanoparticle has no chance of survive in an aluminum melt at the temperatures reached in L-PBF process, even with very rapid process kinetics and under

rather favorable conditions for its preservation. Overall, the curves shown in Figure 10 are consistent with what has been observed experimentally, namely that only the 4.5 µm SiC can be partially preserved.

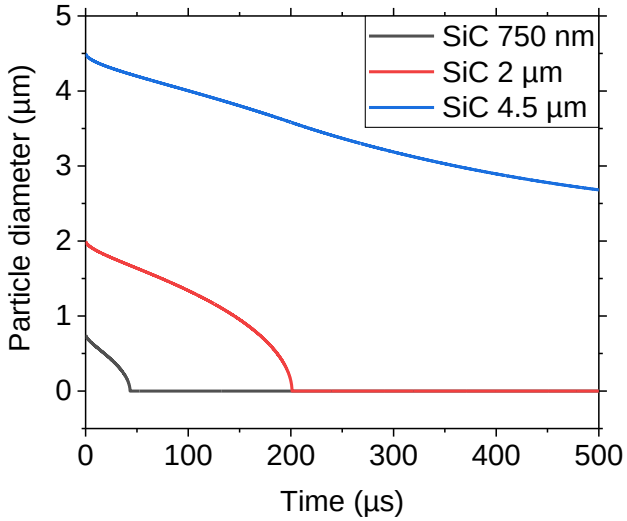

Fig. 10 Evolution of particle size during the process for different starting SiC particle sizes

Another point to investigate is the influence of the different process parameters, the most important being the maximum temperature reached and the time spent in the SiC dissolution range.

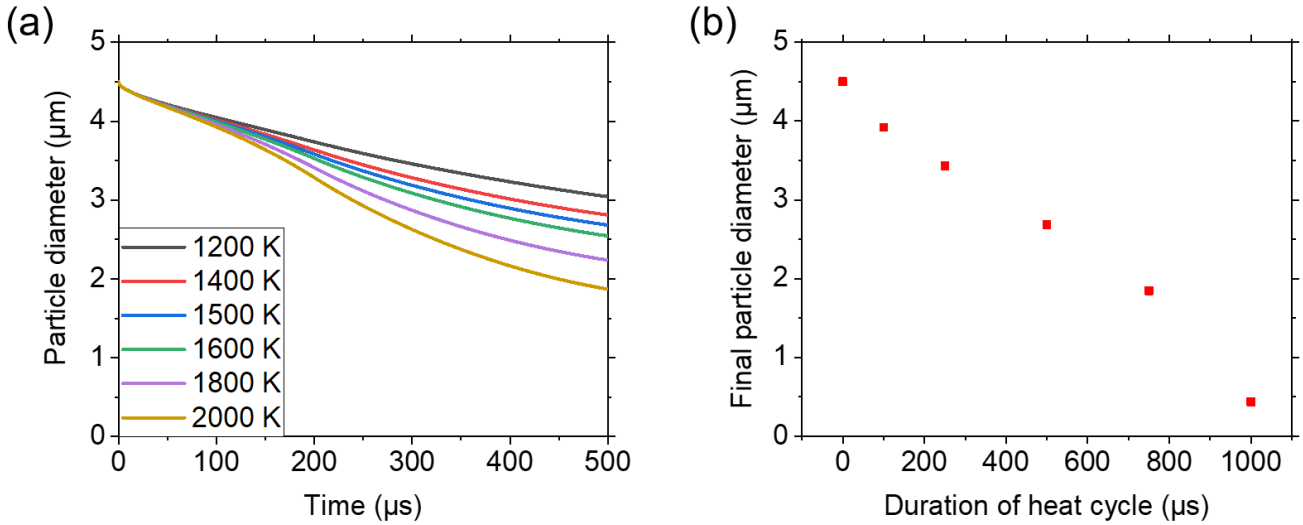

Fig. 11 Influence of maximum temperature (a) and duration of heat cycle t_{End} (b) on the dissolution of a 4.5 µm SiC particle

Figure11-a shows that the maximum temperature of the cycle does not have a great importance on the dissolution of SiC, since a passage from 1200 K to 2000 K only decreases the particle

size of SiC by an additional 1 µm. On the other hand, on Figure11-b, a great sensitivity to the duration of the dissolution cycle is evidenced. Last but not least, the sensitivity of the dissolution process to the diffusion coefficient at 1000 K was studied. The results show a strong dependence, even going as far as a total dissolution of the SiC 4.5 µm for 7.10^{-9} $m^2.s^{-1}$, see Figure 12. This result makes it possible to estimate, from the residual SiC size observed experimentally, that the carbon diffusion coefficient in the $AlSi_7Mg_{0.6}$ melt should be between 3.10^{-9} and 5.10^{-9} $m^2.s^{-1}$.

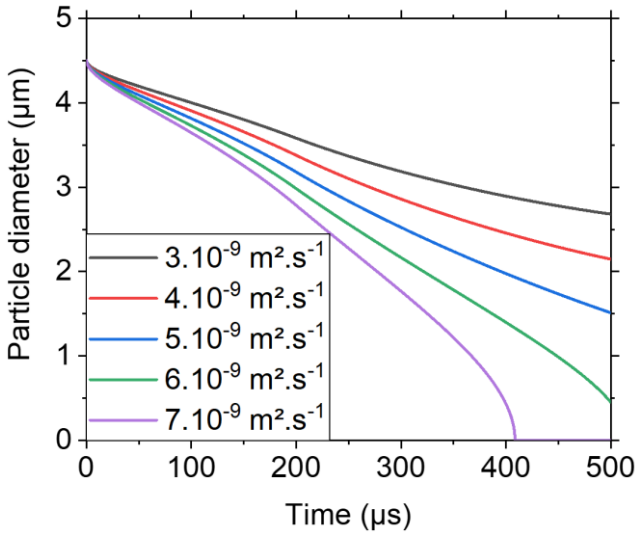

Fig. 12 Influence of diffusion coefficient at 1000 K

Interestingly, all simulation data points can be made to fall on a single master curve using reduced variables for the diffusion budget $(D_{eq}.t)^{1/2}/R_0$ and the particle size $(R_0-R(t))/R_0$, see Figure 13. This result was not a priori obvious, but can be to some extent explained by the fact that the analytical solutions obtained in the short and long times limits (see Appendix 2 for details) can both be expressed using these reduced variables. Quite surprisingly, the composite curve obtained by adding those asymptotic solutions and represented as solid black data in Figure 13 is a fairly good predictor of the data points.

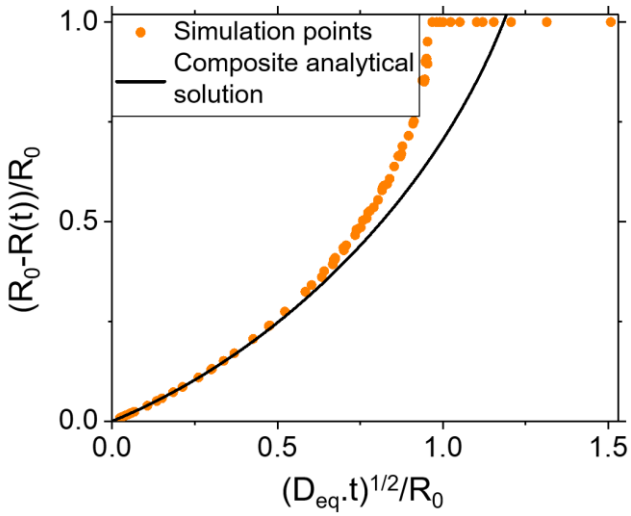

Fig. 13 Simulation points and composite analytical solution

5. Discussion

This dissolution model, even if it is based on several strong approximations, allows to draw some conclusions. It especially demonstrates that sub-micron SiC particles cannot survive the L-PBF process, whatever the parameters chosen. For larger particles of a few micrometers, some SiC may expected to survive depending on diffusion coefficient values. These findings need to be discussed in connection with existing literature data, which presents conflicting results. In particular, some studies are not in agreement with our model and experimental results. M. Wang et al. [12] introduced 2wt% of SiC nanoparticles of 40 nm in an $AlSi_7Mg$ powder matrix. After L-PBF process, they observed nano-sized Al_4C_3, but also residual agglomerated SiC particles by means of SEM and TEM analysis. Using an $AlSi_{10}Mg$ matrix powder with an addition of 2vol% SiC nanoparticles of 40 nm, Z. Wang et al. [11] also detect residual SiC agglomerated and Al_4C_3 by means of Electron Back Scattered Diffraction (EBSD) with phase distribution cartography. Resulting bulk materials are dense, indicating that residual SiC do not comes from lack of fusion. These results are surprising as the dissolution model established in this work indicates that nanoscale SiC cannot survive the process. The fact that they obtained a bulk material with residual SiC is probably related to the fact that SiC agglomerates have been formed due to their large specific surface, and that the liquid aluminum has not succeeded in penetrating these agglomerates. The decomposition of SiC was thus limited and some SiC was preserved.

Some studies also relate to the addition of micrometric SiC reinforcements in aluminum alloys. Their results agree with those of this study, both experimentally and by simulation. They observe large residual SiC particles, as well as the formation of Al_4C_3, showing a partial decomposition of SiC [14–18]. For instance, F. Chang et al. [15] studied the influence of starting SiC particle size in a composite $AlSi_{10}Mg$/20wt%SiC, with SiC particle sizes of 5 µm, 15 µm and 50 µm. In all the dense materials obtained after L-PBF process, residual SiC is observed. They noticed that the extent of SiC decomposition was enhanced by the diminution of SiC particle size.

Another important point to note is the fact that all existing literature data agrees on the fact that it is impossible to elaborate an Al/SiC composite by L-PBF without decomposing at least some of the SiC into aluminum carbide. Even if SiC can be preserved, there is always presence of aluminum carbide, with potentially deleterious effects on parts properties. If we now take a somewhat higher perspective from our present SiC dissolution problem in Al based liquid alloys, an interesting question can be raised on the larger issue of the elaboration of metal based composites manufacturing by L-PBF.

It is of course always dangerous to make clear cut statements on such difficult problems, but our claim is that in thermodynamically unstable systems, a significant added particle dissolution will be unavoidable in practice. Indeed, since the diffusion coefficients in liquid metals do not vary over order of magnitudes, it is expected that, unless strongly agglomerated, truly nanometer particles have little chances of surviving the L-PBF process. In any case, to further quantify matters if necessary, the methodology developed in the present work could be adapted to other metallurgical systems.

The important issue that remains to be addressed pertains to the validity of a diffusion based model in an experimental situation featuring strong fluid flows, with fluid velocities at the melt pool scale in the $m.s^{-1}$ or more range, see e.g [45]. Thus convective mass transport could have been expected to be dominant, invalidating the proposed diffusion based model. However, it has been shown in the related convecto-diffusive problem in crystal growth configurations that what matters for mass transport issues is the value of the fluid velocity V_c taken at the solutal boundary layer edge δ, and that δ is generally much smaller than the melt pool scale [46], as it admits as upper bound the particle size.

In this respect, another finding of the analysis of the convector-diffusive problem in crystal growth configurations is that in the vicinity of a solid boundary, arguments based on the continuity equation show that the relevant fluid velocity should to the first order scale as the square of the distance to that boundary [47]. Now if all results are summarized as a boundary layer Peclet number $Pe_\delta = V_c(\delta).\delta/D$ that measures the relative importance of convective and diffusive mass transport, order of magnitude calculations using as inputs $\delta = 1$ µm, $V_c(\delta) = 100$ µm.s^{-1} and $D = 3.10^{-9}$ m².s^{-1} show that the boundary layer Peclet number Pe_δ takes values smaller than 0.1, meaning that convective transport could be safely neglected. It is of course always questionable to draw clear cut conclusions on the basis of such order of magnitude analysis, but our claim is that for our present problem of dissolution of micron sized particles in L-PBF configurations a diffusion controlled solute transport model is not unreasonable.

6. Conclusion

Our purpose in the present work was to address the issue of the SiC dissolution kinetics in Al-based alloys during L-PBF fabrication, with the objective of preventing or at least limiting SiC decomposition into Al_4C_3. To do so, we first prepared Al/SiC powder composites with SiC particles of various sizes, namely from circa 35 nm to 4.5 µm, using a standard $AlSi_7Mg_{0.6}$ alloy as host material. These powders were then used in a standard L-PBF printer, and the fabricated parts thoroughly characterized. In parallel, a diffusion model has been numerically implemented to simulate SiC dissolution as a function of process conditions. The main findings are summarized as follows:

(1) A standard Turbula mixer allows to ensure a satisfying grip of submicronic sized SiC particles on $AlSi_7Mg_{0.6}$ host powders. The dry coating using 2 µm and 4.5 µm sized SiC particles is poorly efficient because of a too large guest particle size. The use of a more energetic Cyclomix mixer for the 4.5 µm sized SiC particles allows nevertheless a more homogeneous powder mixture than the Turbula mixer.

(2) For all process conditions allowing to avoid lack of fusion porosity, the SiC reinforcements of respectively 35 nm, 750 nm and 2 µm were totally consumed, while part of the 4.5 µm SiC could be preserved.

(3) The diffusion model shows that a 35 nm SiC nano-reinforcement is almost instantaneously dissolved, and that a submicron sized SiC reinforcement cannot survive the process.

We believe that these findings can be extended to cases beyond the Al/SiC problem studied in the present work, leading to the general conclusion that, unless strongly agglomerated, thermodynamically unstable nanoparticles cannot survive the L-PBF process. In any case, provided adequate thermophysical and process parameters can be identified, the numerical simulation methodology we proposed can likely be applied to other metallic systems.

Regarding perspectives, it would be interesting to estimate the residual SiC quantity by selective acid dissolution according to N. Samer et al. work [48]. The most important perspective is to mitigate the negative effects of SiC dissolution in Al based systems. To do so would require to identify a chemical element with higher affinity for C than Al that could be additionally grafted to the Al/SiC composite powders. In this respect, promising results have been obtained using Zr in a related welding configuration [49]. It would of course be necessary to check whether the rather complex dissolution-rearrangement scheme could efficiently take place during the L-PBF process, but the methodology proposed in the present paper could again be implemented in future works.

Appendix 1: Numerical methodology

Our purpose here is to propose a methodology to solve numerically the governing equation for the dissolution process, written as:

$$dR/dt = - (C_I - C_\infty) [R^{-1} + (\pi.D_{eq}(t).t)^{-1/2}] D(T(t)) \quad (5)$$

and subjected to the initial condition $R = R_0$ at $t = 0$. For our present Al-SiC system, the concentrations at the particle interface and far from the particle are respectively fixed at 0.3 and 0 wt%, but it should be noted that the problem is linear in terms of $(C_I - C_\infty)$. To do so the following algorithm is implemented:

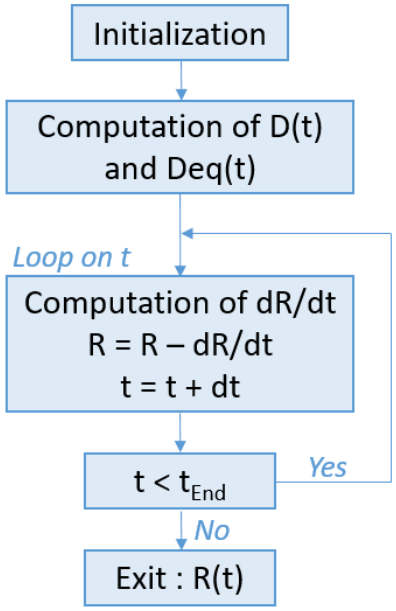

Fig. 14 Algorithm box

In practice, the following steps are implemented:

- Initialization: the user can change several parameters, which he defines at the beginning. He thus firstly defines the temperature profile, and can then set parameters such as the initial size of the particle, choose a method for calculating the temperature dependence of the diffusion coefficient and set the parameters associated with these laws.

- Computation of diffusion coefficients:
    - Determination of the instantaneous diffusion coefficient from the law chosen by the user and the temperature profile, for each given time t.
    - Determination of the equivalent diffusion coefficient taking into account the thermal history of the material, for each given time t.
- In the time loop, calculation of the loss of radius at each t, update of particle radius and increment of time using equation (Figure 14).

The simulations were found to run smoothly with a time step set at 0.05 µs, and typically take less than 10 seconds on a desktop computer.

Appendix 2: Approximate analytical solution

Interestingly, the governing equation (5) admits closed form solutions in the two limiting cases where the particle radius is either very small or very large compared to the characteristic diffusion length:

Case 1: For short times, when the thickness of the diffusive layer is significantly lower than the radius of the particle. In other words, when R remains close to R_0. Under these conditions, the 1/R term in the differential equation can be neglected, allowing to write equation (5) as:

$$dR/dt = - (C_I - C_\infty) (\pi.D_{eq}(t).t)^{-1/2}.D(T(t)) \quad (6)$$

The integration of this equation using as initial condition $R = R_0$ at $t = 0$ allows to obtain eq.(7), the analytical solution valid for short times:

$$(R_0-R)/ R_0 = 2(C_I-C_\infty).\xi /\pi^{1/2} \quad (7)$$

$$\text{with } \xi = (D_{eq}(t)t)^{1/2}/R_0 \quad (8)$$

Case 2: For long times, at the end of dissolution, when the radius of the particle tends toward 0, the $(\pi.Deq(t).t)^{-1/2}$) term can be neglected, yielding:

$$dR/dt = - (C_I - C_\infty).R^{-1}.D(T(t)) \quad (9)$$

The integration of the above equation is mathematically straightforward, but the problem is to assign a proper initial condition. Indeed, since the process has been going on for a while before reaching the long time domain, it is not physically right to state the initial condition as $R = R_0$ at $t = 0$. Taking nevertheless this initial condition for want of a better option, the analytical solution for long times is obtained:

$$(R_0-R)/ R_0 = 1-[1-2(C_I-C_\infty).\xi^2]^{1/2} \quad (10)$$

Both asymptotic solutions are shown in figure 15 along with the numerical data points from the parametric study. As expected, the short time solution is seen to nicely represent the tangent to

the data set in the vicinity of the origin. The situation is not so easily interpreted in the case of the long term solution due to the difficulty in assigning a proper initial condition. Nevertheless it is interesting to see that the long term solution properly accounts fort he curvature of the data set. This may explain why the composite solution built by adding eqs. (7) and (10) provides a decent fit tot he data over all the investigated range.

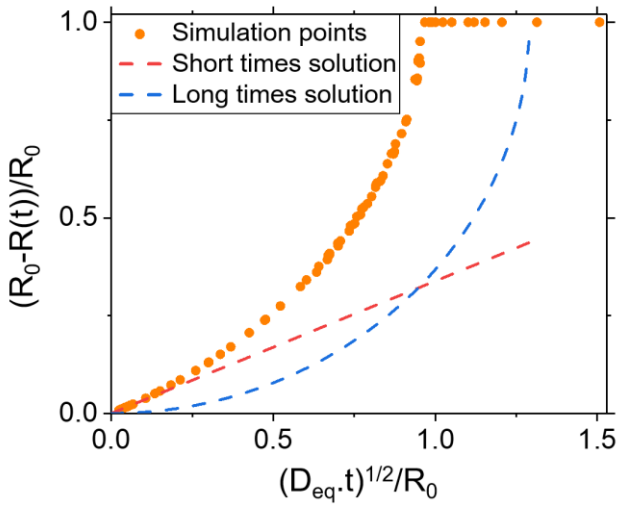

Fig. 15 Simulation points and asymptotic analytical solutions

Acknowledgments

The authors acknowledge the assistance of Céline Ribière for the 3D printing experiments, and Nathalie Ladrat for the FIB lamella preparation.

Funding sources

Financial support from the cross cutting CEA program ‘Matériaux et Procédés’ is gratefully acknowledged.

Conflicts of interest or competing interests

The authors declare that they have no known competing financial interests or personal relationship that could have appeared to influence the work reported in this paper.

Data and code availability

Not applicable.

Supplementary information

More details on the numerical implementation of the model can be found in Appendix 1. Appendix 2 presents more details about the analytical solutions obtained in the short and long times limits.

Ethical approval

This research did not contain any studies involving animal or human participants, nor did it take place on any private or protected areas.

References

1. DebRoy T, Wei HL, Zuback JS, et al (2018) Additive manufacturing of metallic components – Process, structure and properties. Prog Mater Sci 92:112–224. https://doi.org/10.1016/j.pmatsci.2017.10.001

2. Gupta AK, Lloyd DJ, Court SA (2001) Precipitation hardening in Al–Mg–Si alloys with and without excess Si. Mater Sci Eng A 316:11–17. https://doi.org/10.1016/S0921-5093(01)01247-3

3. Pramod SL, Bakshi S, Murty B (2015) Aluminum-Based Cast In Situ Composites: A Review. J Mater Eng Perform 24:. https://doi.org/10.1007/s11665-015-1424-2

4. Li X, Yang Y, Weiss D (2008) Theoretical and experimental study on ultrasonic dispersion of nanoparticles for strengthening cast Aluminum Alloy A356. Metall Sci Technol 26–2:12–20

5. Skibo MD, Schuster DM (1988) Process for production of metal matrix composites by casting and composite therefrom (US4759995A), United States Patent

6. Sweet GA, Brochu M, Hexemer RL, et al (2015) Consolidation of aluminum-based metal matrix composites via spark plasma sintering. Mater Sci Eng A 648:123–133. https://doi.org/10.1016/j.msea.2015.09.027

7. Narciso J, García-Cordovilla C, Louis E (1992) Reactivity of thermally oxidized and unoxidized SiC particulates with aluminium-silicon alloys. Mater Sci Eng B 15:148–155. https://doi.org/10.1016/0921-5107(92)90047-D

8. Gröbner J, Lukas HL, Aldinger F (1996) Thermodynamic calculation of the ternary system Al-Si-C. Calphad 20:247–254. https://doi.org/10.1016/S0364-5916(96)00027-2

9. Gu D, Chang F, Dai D (2015) Selective Laser Melting Additive Manufacturing of Novel Aluminum Based Composites With Multiple Reinforcing Phases. J Manuf Sci Eng 137:021010. https://doi.org/10.1115/1.4028925

10. Salvo L, L'Espérance G, Suéry M, Legoux JG (1994) Interfacial reactions and age hardening in Al-Mg-Si metal matrix composites reinforced with SiC particles. Mater Sci Eng A 177:173–183. https://doi.org/10.1016/0921-5093(94)90489-8

11. Wang Z, Zhuo L, Yin E, Zhao Z (2021) Microstructure evolution and properties of nanoparticulate SiC modified AlSi10Mg alloys. Mater Sci Eng A 808:140864. https://doi.org/10.1016/j.msea.2021.140864

12. Wang M (2019) Improved mechanical properties of AlSi7Mg/nano-SiCp composites fabricated by selective laser melting. J Alloys Compd 810:151926. https://doi.org/10.1016/j.jallcom.2019.151926

13. Xue G, Ke L, Zhu H, et al (2019) Influence of processing parameters on selective laser melted SiCp/AlSi10Mg composites: Densification, microstructure and mechanical

properties. Mater Sci Eng -Struct Mater Prop Microstruct Process 764:138155. https://doi.org/10.1016/j.msea.2019.138155

14. Zou T, Mei S, Chen M, Zhu H (2022) Influence of SiC Content on Microstructure and Mechanical Properties of SiCp/AlSi7Mg Composites Fabricated by Selective Laser Melting. J Mater Eng Perform. https://doi.org/10.1007/s11665-022-07079-7

15. Chang F, Gu D, Dai D, Yuan P (2015) Selective laser melting of in-situ Al4SiC4+SiC hybrid reinforced Al matrix composites: Influence of starting SiC particle size. Surf Coat Technol 272:15–24. http://dx.doi.org/10.1016/j.surfcoat.2015.04.029

16. Astfalck LC, Kelly GK, Li X, Sercombe TB (2017) On the Breakdown of SiC during the Selective Laser Melting of Aluminum Matrix Composites. Adv Eng Mater 8:1600835. https://doi.org/10.1002/adem.201600835

17. Xie H, Zhang J, Li F, et al (2021) Selective laser melting of SiCp/Al composites: Densification, microstructure, and mechanical and tribological properties. Ceram Int 47:30826–30837. https://doi.org/10.1016/j.ceramint.2021.07.263

18. Zhang D, Yi D, Wu X, et al (2022) SiC reinforced AlSi10Mg composites fabricated by selective laser melting. J Alloys Compd 894:162365. https://doi.org/10.1016/j.jallcom.2021.162365

19. Pfeffer R, Dave RN, Wei D, Ramlakhan M (2001) Synthesis of engineered particulates with tailored properties using dry particle coating. Powder Technol 117:40–67. https://doi.org/10.1016/S0032-5910(01)00314-X

20. Soulier M, Benayad A, Teulon L, et al (2022) Nanocomposite powder for powder-bed-based additive manufacturing obtained by dry particle coating. Powder Technol 404:117474. https://doi.org/10.1016/j.powtec.2022.117474

21. Sow MC, De Terris T, Castelnau O, et al (2020) Influence of beam diameter on Laser Powder Bed Fusion (L-PBF) process. Addit Manuf 36:101532. https://doi.org/10.1016/j.addma.2020.101532

22. Yadav P, Rigo O, Arvieu C, Lacoste E (2022) Microstructural and mechanical aspects of AlSi7Mg0.6 alloy related to scanning strategies in L-PBF. Int J Adv Manuf Technol 120:6205–6223. https://doi.org/10.1007/s00170-022-09127-x

23. Huang S, Guo S-Q, Zhou B, et al (2021) Microstructure and properties of AlSi7Mg alloy fabricated by selective laser melting. China Foundry 18:416–423. https://doi.org/10.1007/s41230-021-1004-z

24. Liang L, Pan X, Wang G, et al (2021) Microstructure and mechanical properties of selective laser melted AlSi7Mg. In: Journal of Physics: Conference Series. p 012041

25. Spierings A, Schneider M, Eggenberger R (2011) Comparison of Density Measurement Techniques for Additive Manufactured Metallic Parts. Rapid Prototyp J 17:380–386. https://doi.org/10.1108/13552541111156504

26. De Terris T, Andreau O, Peyre P, et al (2019) Optimization and comparison of porosity rate measurement methods of Selective Laser Melted metallic parts. Addit Manuf 28:802–813. https://doi.org/10.1016/j.addma.2019.05.035

27. Yang J, Sliva A, Banerjee A, et al (2005) Dry particle coating for improving the flowability of cohesive powders. Powder Technol 158:21–33. https://doi.org/10.1016/j.powtec.2005.04.032

28. Oguchi T, Tamatani M (1986) Contact Electrification in Inorganic Binary Compounds. J Electrochem Soc 133:841–847. https://doi.org/10.1149/1.2108690

29. Li XP, O'Donnell KM, Sercombe TB (2016) Selective laser melting of Al-12Si alloy: Enhanced densification via powder drying. Addit Manuf 10:10–14. https://doi.org/10.1016/j.addma.2016.01.003

30. Saunders M (2019) X marks the spot - find the ideal process parameters for your metal AM parts. Renishaw Plc. https://www.renishaw.com/resourcecentre/en/details/--106810

31. Snow Z, Nassar AR, Reutzel EW (2020) Invited Review Article: Review of the formation and impact of flaws in powder bed fusion additive manufacturing. Addit Manuf 36:101457. https://doi.org/10.1016/j.addma.2020.101457

32. Seager RJ, Acevedo AJ, Spill F, Zaman MH (2018) Solid dissolution in a fluid solvent is characterized by the interplay of surface area-dependent diffusion and physical fragmentation. Sci Rep 8:7711. https://doi.org/10.1038/s41598-018-25821-x

33. Crank J (1956) The Mathematics of Diffusion. In: Clarendon Press, Oxford

34. Maclean DJ, Alboussière T (2001) Measurement of solute diffusivities. Part I. Analysis of coupled solute buoyancy-driven convection and mass transport. Int J Heat Mass Transf 44:1639–1648. https://doi.org/10.1016/S0017-9310(00)00308-2

35. Garandet JP, Praizey JP, Van Vaerenbergh S, Alboussiere T (1997) On the problem of natural convection in liquid phase thermotransport coefficients measurements. Phys Fluids 9:510–518. https://doi.org/10.1063/1.869215

36. Mathiak G, Griesche A, Kraatz KH, Frohberg G (1996) Diffusion in liquid metals. J Non-Cryst Solids 205–207:412–416. https://doi.org/10.1016/S0022-3093(96)00253-0

37. Botton V, Lehmann P, Bolcato R, et al (2001) Measurement of solute diffusivities. Part II. Experimental measurements in a convection-controlled shear cell. Interest of a uniform magnetic field. Int J Heat Mass Transf 44:3345–3357. https://doi.org/10.1016/S0017-9310(00)00362-8

38. Liu Y, Lin W, Zhou B, et al (2022) Ex-situ study of diffusion in liquid Al–Cu melts under a transverse magnetic field using X-ray imaging. Philos Mag Lett 102:151–159. https://doi.org/10.1080/09500839.2022.2048111

39. Du Y, Chang YA, Huang B, et al (2003) Diffusion coefficients of some solutes in fcc and liquid Al: critical evaluation and correlation. Mater Sci Eng A 363:140–151. https://doi.org/10.1016/S0921-5093(03)00624-5

40. Kargl F, Weis H, Unruh T, Meyer A (2012) Self diffusion in liquid aluminium. J Phys Conf Ser 340:012077. https://doi.org/10.1088/1742-6596/340/1/012077

41. Sondermann E, Kargl F, Meyer A (2016) Influence of cross correlations on interdiffusion in Al-rich Al-Ni melts. Phys Rev B 93:184201. https://doi.org/10.1103/PhysRevB.93.184201

42. Sondermann E, Jakse N, Binder K, et al (2019) Concentration dependence of interdiffusion in aluminum-rich Al-Cu melts. Phys Rev B 99:024204. https://doi.org/10.1103/PhysRevB.99.024204

43. Li Y, Gu D (2014) Parametric analysis of thermal behavior during selective laser melting additive manufacturing of aluminum alloy powder. Mater Des 63:856–867. https://doi.org/10.1016/j.matdes.2014.07.006

44. Loh L-E, Chua C-K, Yeong W-Y, et al (2015) Numerical investigation and an effective modelling on the Selective Laser Melting (SLM) process with aluminium alloy 6061. Int J Heat Mass Transf 80:288–300. https://doi.org/10.1016/j.ijheatmasstransfer.2014.09.014

45. Ly S, Rubenchik AM, Khairallah SA, et al (2017) Metal vapor micro-jet controls material redistribution in laser powder bed fusion additive manufacturing. Sci Rep 7:4085. https://doi.org/10.1038/s41598-017-04237-z

46. Garandet JP (1993) Microsegregation in crystal growth from the melt: an analytical approach. J Cryst Growth 131:431–438. https://doi.org/10.1016/0022-0248(93)90192-Y

47. Chatelain M, Rhouzlane S, Botton V, et al (2017) Towards wall functions for the prediction of solute segregation in plane front directional solidification. J Cryst Growth 475:55–69. https://doi.org/10.1016/j.jcrysgro.2017.05.019

48. Samer N, Andrieux J, Gardiola B, et al (2015) Microstructure and mechanical properties of an Al–TiC metal matrix composite obtained by reactive synthesis. Compos Part Appl Sci Manuf 72:50–57. https://doi.org/10.1016/j.compositesa.2015.02.001

49. Long J, Zhang L-J, Zhang L-L, et al (2020) Effects of minor Zr addition on the microstructure and mechanical properties of laser welded joint of Al/SiCp metal-matrix composite. J Manuf Process 49:373–384. https://doi.org/10.1016/j.jmapro.2019.12.004